Nonlocal gap solitons in $\mathcal{PT}$-symmetric periodic potentials with defocusing nonlinearity

Chandroth P. Jisha,[1,*] Alessandro Alberucci,[2] Valeriy A. Brazhnyi,[1] and Gaetano Assanto[2]

[1]*Centro de Física do Porto, Faculdade de Ciências, Universidade do Porto, Rua do Campo Alegre 687, 4169-007 Porto, Portugal*

[2]*Nonlinear Optics and OptoElectronics Lab (NooEL), Via della Vasca Navale 84, 00146 Rome, Italy*

(Received 19 November 2013; published 13 January 2014)

Existence and stability of $\mathcal{PT}$-symmetric gap solitons in a periodic structure with defocusing nonlocal nonlinearity are studied both theoretically and numerically. We find that, for any degree of nonlocality, gap solitons are always unstable in the presence of an imaginary potential. The instability manifests itself as a lateral drift of solitons due to an unbalanced particle flux. We also demonstrate that the perturbation growth rate is proportional to the amount of gain (loss), thus predicting the observability of stable gap solitons for small imaginary potentials.

DOI: 10.1103/PhysRevA.89.013812 PACS number(s): 42.65.Tg, 03.65.Ge, 11.30.Er, 42.70.Qs

I. INTRODUCTION

Systems with a non-Hermitian Hamiltonian possessing a real eigenvalue spectrum gained interest after the early work by Bender *et al*. [1], who showed that the condition of Hermiticity to obtain real eigenvalues can be replaced if the system satisfies an additional condition of parity-time invariance in the form $\mathbf{PTH} = \mathbf{HPT}$, with the additional constraint that $\mathbf{H}$ and $\mathbf{PT}$ share a common set of eigenvectors, with $\mathbf{P}$ and $\mathbf{T}$ parity and time-reversal operators, respectively. Moreover, it was demonstrated that quantum systems encompassing a potential such that $V(x) = V^*(-x)$ satisfy the $\mathcal{PT}$ symmetry. In fact, the eigenvalues remain purely real in a given subset of system parameters: a phase transition towards complex eigenvalues connected with a spontaneous symmetry breaking can be observed [2,3]. Such systems are appealing from both fundamental and practical perspectives, as evident from the vast literature in diverse areas, including quantum mechanics, integrated optics, plasmonics, and metamaterials, among others [4–10].

In optics, where the attention paid to $\mathcal{PT}$ theory has been greater, the interest relies mainly on the fact that the Maxwell equations can be often recast as a Schrödinger equation; the biggest advantage is the ease in realizing complex Hamiltonians both in the spatial [11] and in the temporal domains [12,13] and, consequently, the accessible experimental demonstration of the theoretical findings. Singular light properties such as nonreciprocal photon propagation have been demonstrated, leading to new technological achievements like the realization of an all-optical diode in silicon [14]. The role of nonlinearity has been addressed as well, with the prediction of $\mathcal{PT}$-symmetric solitons [15]. In optical systems, $\mathcal{PT}$-symmetric potentials can be obtained by suitable tailoring of the real and imaginary parts of the refractive indices, such that the real part is a symmetric function with position and the imaginary part encompassing gain and loss terms is antisymmetric in space (including metal insertions [3,14] and pumped system [11,16]); in matter-wave systems $\mathcal{PT}$-symmetric potentials can be achieved by suitable gain and loss mechanisms introduced through coupling with external reservoirs.

On the other hand, in the past decade attention has been paid to waveguide arrays and the formation of discrete solitons [17,18], including spatial gap solitons [19,20], that is, self-localized nonlinear waves with a propagation constant within the linear band gap of the periodic structure. Light propagation through $\mathcal{PT}$-symmetric periodic potentials, including exotic phenomena such as $\mathcal{PT}$-symmetry breaking, nonreciprocal behavior, and double refraction, were investigated from the beginning, in both the linear and nonlinear regimes [15,21,22]. The existence of $\mathcal{PT}$-symmetric solitons and breathers was also discussed in the context of couplers and array geometries [23]. The existence and stability of two-dimensional gap solitons in $\mathcal{PT}$ linear lattices with a local Kerr response was discussed in Ref. [24].

While stable gap solitons can exist in $\mathcal{PT}$-symmetric linear periodic potentials in nonlinear defocusing local media, the role of nonlocality on the stability and mobility of localized solutions is still an open issue. Recently, studies were reported on solitons in $\mathcal{PT}$-symmetric periodic potentials in nonlocal self-focusing media [25] and in the presence of linear defects [26], as well as on nonlocal bright solitons in defocusing media [27], including geometries with localized $\mathcal{PT}$-symmetric potentials [28]. Nevertheless, the effect of nonlocality on gap solitons in $\mathcal{PT}$-symmetric periodic potentials with self-defocusing has not been addressed to date.

In the present work, we study the existence and stability of $\mathcal{PT}$-symmetric gap solitons in defocusing nonlocal media in the presence of a periodic potential and with a diffusive-like nonlinear response, such as that exhibited by, e.g., nematic liquid crystals [18,29], thermo-optic materials [30], and atomic vapors [31]. While stationary modes are obtained only on-site (i.e., corresponding to potential minima) due to lack of parity symmetry for the overall system, we demonstrate that gap solitons in $\mathcal{PT}$ potentials are always unstable for any degree of nonlocality, generally undergoing oscillatory instabilities (OIs). Multicomponent and multiparameter systems as well as dissipative systems are commonly associated with OIs, the latter originally discussed in the context of parametrically driven damped Kerr media [32] and later extended to the generalized Thirring model [33,34] and other systems [35,36]. It is to be noted that the existence of OIs in Hermitian systems results in the eventual decay or blow-up of the stationary solution [33,36]. Here we demonstrate that the existence of OIs in $\mathcal{PT}$-symmetric systems leads to unidirectional energy

*Corresponding author: cpjisha@gmail.com

transfer from one lattice site to the other, specifically from the loss regions towards the gain regions.

II. DEFOCUSING NONLOCAL GAP SOLITONS IN THE BAND-GAP REGION

We consider a generic field Ψ describing either the particle distribution for matter waves or the electric field for light (electromagnetic) waves. We further assume that the material is linearly inhomogeneous and can be modeled by a linear periodic potential $V(x)$ with a nonvanishing imaginary part [21]. Finally, we study a nonlocal nonlinear medium with a diffusive response. The evolution of the field Ψ versus propagation z (time for matter waves, propagation distance for light) obeys the following system:

$$i\frac{\partial\Psi}{\partial z} = -\frac{1}{2}\frac{\partial^2\Psi}{\partial x^2} + V(x)\Psi + V_{\rm NL}(|\Psi|^2)\Psi, \tag{1}$$

$$V_{\rm NL} - \sigma\frac{\partial^2 V_{\rm NL}}{\partial x^2} = |\Psi|^2, \tag{2}$$

where x is the transverse coordinate and $V_{\rm NL}$ is the nonlinear portion of the complete potential $V + V_{\rm NL}$. Equation (1) is the well-known Gross-Pitaevskii equation (i.e., nonlinear Schrödinger equation in optics), whereas Eq. (2) is in the form of a screened Poisson or Yukawa equation. The parameter σ (defined as a strictly positive quantity) determines the range of nonlocality: a large σ corresponds to a highly nonlocal response [37]; in particular, the width d of the Green function $G(x)$ of Eq. (2) is proportional to $\sqrt{\sigma}$, with $G(x) = -1/(2\sqrt{\sigma})\exp(-|x|/\sqrt{\sigma})$. In writing Eq. (2) we assumed a self-defocusing Kerr medium as $V_{\rm NL}$ is proportional to the intensity $|\Psi|^2$: a bell-shaped Ψ gives rise to a repulsive potential. For the potential to be $\mathcal{PT}$ symmetric, a necessary (but not sufficient) condition is that $V(x) = V^*(-x)$ [11]: hereby we make the ansatz $V(x) = V_r(x) + iV_i(x) = V_r\sin^2(x) - iV_i\sin(2x)$, setting to π the period of the linear potential without any loss of generality.

We look for propagation-invariant solutions of Eqs. (1) and (2) in the form $\Psi(x,z) = \phi(x)\exp(-i\mu z)$, $-\mu$ being the propagation constant for light waves or μ the chemical potential for matter waves. The substitution into Eqs. (1) and (2) provides the nonlinear eigenvalue problem

$$\mu\phi = -\frac{1}{2}\phi_{xx} + [V_r\sin^2(x) - iV_i\sin(2x)]\phi + V_{\rm NL}\phi, \tag{3}$$

$$V_{\rm NL} - \sigma\frac{\partial^2 V_{\rm NL}}{\partial x^2} = |\phi|^2. \tag{4}$$

A. Linear eigenmodes

The linearized version of Eq. (3) (i.e., with $V_{\rm NL} = 0$) supports Bloch waves of the form $\phi_K(x) = u_K(x)\exp(iKx)$ [38], where $u_K(x+\pi) = u_K(x)$, i.e., u is a π-periodic function of x. Figure 1 shows the behavior of the linear eigenvalues μ versus the real potential V_r for purely real ($V_i = 0$) and for $\mathcal{PT}$-symmetric ($V_i \neq 0$) potentials [15]. For $V_i = 0$ the number and size of the band gaps increase with V_r due to the stronger confinement in each lattice site. For $V_i \neq 0$ the two lowest bands merge for small V_r (inside the shaded region), corresponding to the breakup of the $\mathcal{PT}$ symmetry: the eigenvalues μ belonging to this band are complex. When V_r overcomes a threshold, dependent on V_i and explicitly given by $V_r = 2V_i$, the two lowest bands split, the $\mathcal{PT}$ symmetry is fulfilled, and the eigenvalues become purely real [15,21], corresponding to the unshaded region in Fig. 1.

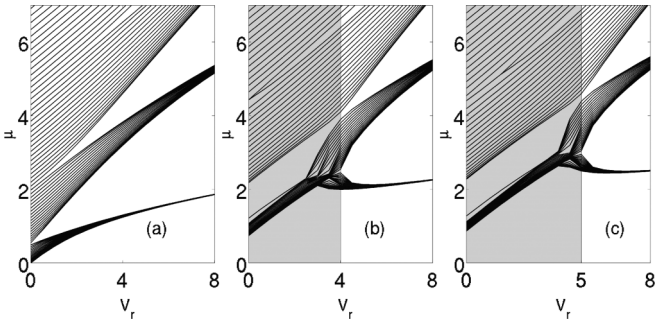

FIG. 1. Real part of the eigenvalue μ vs V_r with the imaginary part V_i of the $\mathcal{PT}$-symmetric potential taking the values (a) 0, (b) 2, and (c) 2.5, respectively. The energy spectrum has complex eigenvalues in the shaded region.

The eigenvalue spectrum for the free-particle case, i.e., in the absence of any potential, follows $\mu = K^2/2$. As is well known, for $V_i = 0$ the system spectrum exhibits gaps; in particular, for $V_r = 4$, there are two finite band gaps for $\mu < 8$ [thickest line in Fig. 2(a)]. Figure 2 graphs the dependence of the dispersion relation on the imaginary part V_i of the potential when V_r is arbitrarily fixed to 4, together with the free-particle case (lowest curve). Starting from $V_i = 0$ and then increasing V_i [see Figs. 2(c) and 2(d)], the eigenvalue spectrum remains real ($\mathcal{PT}$ symmetry is conserved) until $V_i = V_r/2 = V_c$, where the potential reduces to $V(x) = V_r[1 - \exp(2ix)]/2$: thus, for $V_i = V_c$ the energy band gaps disappear, resulting in a spectrum equivalent to that of a free particle, but shifted above

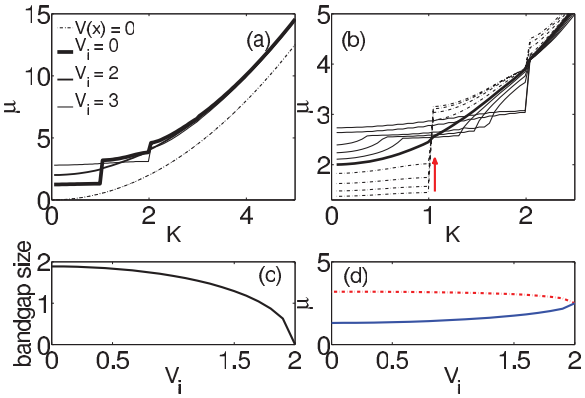

FIG. 2. (Color online) Dispersion relation for $V_r = 4$. (a) Real part of μ for V_i varying from 0 to 3 (thicker to thinner lines). The bottom line shows the free-particle case. Note the curve for $V_i = 2$, where the band gaps disappear and the dispersion relation follows $\mu = K^2/2 + V_c$: this is the $\mathcal{PT}$-symmetry breaking point. Below this critical point all the eigenvalues are real. (b) Enlargement of the dispersion relation. The arrow indicates the direction of increasing V_i. Dotted lines, $V_i < 2$; thin lines, $V_i > 2$. (c) Band-gap size and (d) μ values at the lower (solid blue line) and upper (dotted red line) band edges vs V_i.

by V_c, i.e., $\mu = K^2/2 + V_c$ [21,27]. Conversely, when $V_i > V_c$ (broken $\mathcal{PT}$ symmetry), the spectrum becomes complex; furthermore, there is no energy band gap in the first Brillouin zone, as the first band gap shifts to the second Brillouin zone [see Fig. 2(b)]. Such symmetry breaking in the spectrum was discussed in detail in Refs. [15,21,39].

For $V_i = V_c$ and neglecting the nonlinearity, the Floquet mode $u_K(x)$ obeys (up to the end of the section we consider a potential of period T in order to generalize our result)

$$\mu u_K = -\frac{1}{2}\frac{\partial^2 u_K}{\partial x^2} + \frac{V_r + K^2}{2} u_K - iK\frac{\partial u_K}{\partial x} - \frac{V_r e^{\frac{2\pi i x}{T}}}{2} u_K \tag{5}$$

with $T = \pi$ in our case. Equation (5) can be solved by expressing $u_K(x)$ in its Fourier series as $u_K(x) = \sum_{n=-\infty}^{\infty} a_n(K) e^{\frac{2\pi i n x}{T}}$. After defining $G = K + 2\pi n/T$, a direct substitution into Eq. (5) provides the recursive relation

$$\left(\frac{V_r + G^2}{2} - \mu\right) a_n = \frac{V_r}{2} a_{n-1}. \tag{6}$$

By looking at Eq. (6) it is apparent that, if $(\frac{V_r+G^2}{2} - \mu) \neq 0$, when one of the coefficients a_n vanishes then all a_n go to zero, leading to the trivial solution $u_K = 0$. Hence, nontrivial Bloch modes exist only if $G^2 = 2\mu - V_r$, with G^2 spanning all the positive half of the real axis; thus, the eigenvalue μ has to satisfy the necessary condition

$$\mu > \frac{V_r}{2} = V_c. \tag{7}$$

For a fixed pair (μ, K) we have a nonzero $u_K(x)$ if there is a given $\overline{n}(\mu, K)$ such that $0.5\,(K + 2\pi\overline{n}/T)^2 = \mu - V_r/2$; then the expansion coefficients $a_n(\mu, K)$ are zero for $n < \overline{n} - 1$, whereas for $n > \overline{n} - 1$ they can be computed via Eq. (6). Summarizing, the system shows a continuous spectrum with a cutoff at $\mu = V_c$, in agreement with our numerics [27].

For the sake of simplicity and without loss of generality, hereafter we take $V_r = 4$: Fig. 1(b) shows that the transition from a real to a complex spectrum occurs for $V_i = 2$.

B. Nonlinear case

We now concentrate on calculating the form assumed by shape-preserving wave packets in the presence of nonlinearity. As is well known, gap solitons exist only in the linear band gaps (hence the name): we look for fundamental $\mathcal{PT}$-symmetric gap solitons embedded in the first linear band gap by choosing $V_i < V_c$ to avoid symmetry breaking. We also note that, due to the presence of the odd imaginary potential V_i, off-site gap solitons do not exist in our case [40]. Typical profiles of on-site gap solitons, obtained using a pseudospectral technique based on Chebyshev polynomials, are shown in Fig. 3 for various degrees of nonlocality and for μ close to the upper band edge. We set a numerical window much wider than the nonlocal length d to avoid spurious effects from the boundaries [37,41]. Analogously to the case of purely real lattices [40,42], the real component of the fundamental gap soliton is mainly localized in a given guide, with tails extending towards adjacent guides and shaped so that the linear modes

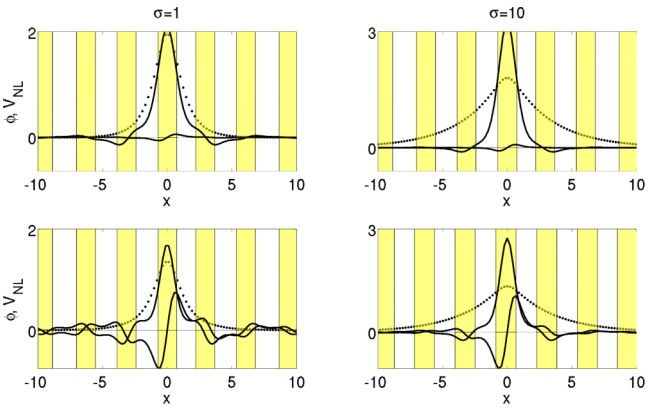

FIG. 3. (Color online) Gap soliton profiles for $\mu = 3$ vs x. The symmetric and antisymmetric curves correspond to the real and imaginary parts, respectively. The dotted lines show the corresponding nonlinear potential $V_{\rm NL}$ for two values of the nonlocality $\sigma = 1$ (left) and $\sigma = 10$ (right). Each row corresponds to $V_i = 0.1$ and 1.5, respectively. The yellow and white boxes sketch the qualitative trend of the linear real potential $V_r(x)$ along x, with midpoints in the yellow and white regions corresponding to minima and maxima of the real potential, respectively; otherwise stated, the yellow regions correspond to the guiding channels.

in these guides are excited in phase opposition with respect to the main lobe [17]. Moreover, regardless of V_i, the larger the nonlocality is the lower the tails are (compare left and right columns in Fig. 3), similar to the case $V_i = 0$ [40]. A physical explanation of this behavior relies on coupled mode theory: to exist, gap solitons require out-of-phase excitation of neighboring guides, with the nonlinear response providing the needed difference in propagation constants (energies for matter waves) between core and side channels. In the local Kerr case, a strong excitation is needed in the adjacent sites to reach the necessary nonlinear phase modulation, whereas in the nonlocal case the nonlinear perturbation induced by the mode in the core guide, spreading outwards owing to the finite size of the Green function $G(x)$, provides the required modulation.

At variance with the case $V_i = 0$, gap solitons have a symmetric real part and an antisymmetric imaginary part in order to fulfill power (number of particles) conservation. In fact, in the presence of a complex potential the particle conservation for the imaginary Schrödinger equation (that is, containing a complex potential) reads

$$\nabla \cdot j = -\frac{\partial \rho}{\partial z} + 2V_i(x)\rho, \tag{8}$$

where $\rho = |\phi|^2$ is the wave intensity and the particle flux j is given by $j = \frac{1}{2i}(\psi^* \frac{\partial \psi}{\partial x} - \psi \frac{\partial \psi^*}{\partial x})$. Setting $\phi = \sqrt{\rho} e^{i\chi(x)}$, the flux reads $j = \rho \frac{\partial \chi}{\partial x}$. Setting $\partial\rho/\partial z = 0$, Eq. (8) yields

$$\frac{\partial}{\partial x}\left(\rho \frac{\partial \chi}{\partial x}\right) = 2V_i(x)\rho. \tag{9}$$

According to Eq. (9), an even ρ corresponds to an odd χ, that is, an even real part and an odd imaginary part, respectively. Physically, particles are created within the gain regions and then they diffuse (transversely) towards the loss regions in order to keep the overall (i.e., integrated along x) particle number constant. Noteworthy, the flux j is an

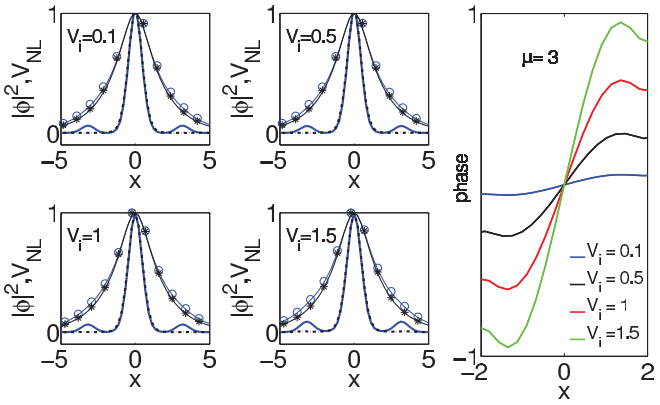

FIG. 4. (Color online) Normalized stationary profiles $|\phi|^2$ (lines) and corresponding nonlinear potential $V_{\rm NL}$ (symbols) for various V_i and $\sigma = 10$ when $\mu = 1.4$, 1.45, 1.6, and 1.9 (lowest μ for each V_i, $\circ$, solid line) and $\mu = 3$ ($*$, dotted line). An increase in μ reduces the soliton tails and makes the solution more and more confined in the channel where initially excited. The last panel shows the phase profile of the solutions when $\mu = 3$; at each x the absolute phase increases with V_i.

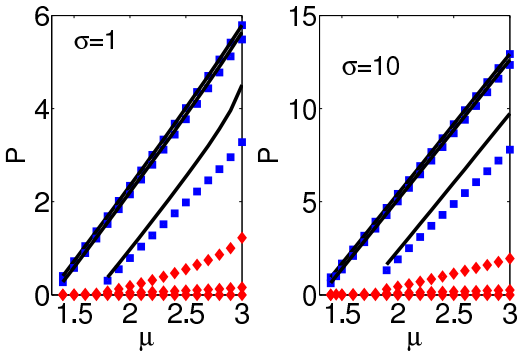

FIG. 5. (Color online) Power P vs μ for $\sigma = 1$ and $\sigma = 10$, respectively. The black solid curves represent the total power P, the blue squares ($\square$) correspond to P_r (top to bottom), and the red diamonds ($\diamond$) correspond to P_i for $V_i = 0$, 0.5, and 1.5, from bottom to top, respectively. Fundamental gap solitons are considered here.

even function; that is, a unidirectional flow takes place [15]. Equation (9) also states that the larger V_i is the larger the antisymmetric part is (see the rightmost panel in Fig. 4), due to the increase in the transverse flux of particles necessary to compensate the inhomogeneous gain or loss. The flux j corresponds in optics to the transverse component of the Poynting vector; see Ref. [15].

Figure 4 elucidates the dependence of the soliton tails on the propagation constant μ, i.e., on the soliton power. For values of μ close to the lower band edge [see Fig. 2(d)], the solitons have pronounced tails (solid lines without symbols in Fig. 4), with the tails diminishing as the eigenvalue μ approaches the upper band edge (dotted lines without symbols in Fig. 4), such dynamics being fully analogous to what happens in a purely real potential [40]. The phases associated with these solutions are illustrated in the last panel of Fig. 4: the phase has a hyperbolic tangent profile in the central region and deviates from it when overlapping with the adjacent guides.

Figure 5 plots the soliton power (number of particles for matter waves), defined as $P = \int |\phi|^2 dx$. First, the soliton power increases with the nonlinear eigenvalue μ, consistently with the self-defocusing nature of the nonlinear response. The power $P_{r,i} = \int |\phi_{r,i}|^2 dx$ carried by the real and the imaginary parts of the solution is also graphed. With increasing magnitude of the complex potential, the power carried by the imaginary part also increases, in turn affecting the stability of the solutions as we demonstrate in the following. We also note that the power carried by the soliton increases with the nonlocality σ due to the lower nonlinear effect (see the form of the Green function G and Ref. [40]), with a ratio P_r/P_i roughly proportional to V_i but slightly dependent on σ.

III. VARIATIONAL APPROACH

Before studying the stability of the solutions, we adopt a variational analysis to look for analytical solutions and verify how well this semianalytical approach predicts the solutions of a $\mathcal{PT}$-symmetric system. Here we apply variational analysis to optical $\mathcal{PT}$-symmetric systems. The semianalytical results using a variational approximation [40,43,44] are obtained from the Lagrangian of the system Eq. (1) for solutions of the form $\Psi(x,z) = \phi(x,z)\exp(-i\mu z)$; for the conservative part the Lagrangian reads

$$L_C = \frac{i}{2}(\phi_z^*\phi - \phi_z\phi^*) - \mu|\phi|^2 + \frac{1}{2}|\phi_x|^2 + V_r\sin^2(x)|\phi|^2 + V_{\rm NL}|\phi|^2 - \frac{\sigma}{2}\left(\frac{\partial V_{\rm NL}}{\partial x}\right)^2 - \frac{V_{\rm NL}^2}{2}. \quad (10)$$

As Fig. 4 shows, the width of the intensity profile does not appreciably vary for increasing μ, the main portion of the wave packet being confined in a single channel. At the same time, the exact soliton profiles have tails which, for μ close to the upper band, become negligibly small. This allows us to choose very general trial functions of the form

$$\phi = A\exp\left(-\frac{x^2}{w_b^2}\right)\exp\left[i\theta(z)f(x)\right], \quad (11)$$

$$V_{\rm NL} = A_{\rm NL}\exp\left(-\frac{x^2}{w_{\rm NL}^2}\right), \quad (12)$$

where A corresponds to the field amplitude, θ is the amplitude of the phase profile, and $f(x)$ is its spatial distribution along x; $A_{\rm NL}$ is the amplitude of the nonlinear potential and, finally, w_b and $w_{\rm NL}$ are the widths of the soliton and of the nonlinear perturbation $V_{\rm NL}$, respectively. Given that the real part of the solution is symmetric and that the imaginary part is antisymmetric, we assume $f(x)$ to be an odd function of x. The nonlocal nonlinear potential well is paraboliclike in the proximity to the soliton and proportional to the Green function of Eq. (2) away from it [i.e., $\exp(-|x|/d)$]; for simplicity we take a Gaussian profile. The phase factor is accounted for in the θ term and, as shown below, can predict the observed behavior of the solutions to a reasonable extent.

The standard variational approach for systems with dissipative terms can be modified as [43,45]

$$\frac{d}{dz}\left(\frac{\partial\langle L_C\rangle}{\partial\beta_z}\right) - \frac{\partial\langle L_C\rangle}{\partial\beta} = 2\,{\rm Re}\int_{-\infty}^{\infty} Q\frac{\partial\phi^*}{\partial\beta}dx, \quad (13)$$

where β stands for all the parameters free to vary in our variational computation (A, $A_{\rm NL}$, P, w_b, $w_{\rm NL}$, θ); we also defined $Q = iV_i \sin(2x)\phi$ and $\langle L_C\rangle = \int_{-\infty}^{\infty} L_C dx$.

Using Eqs. (11) and (12), the reduced Lagrangian is

$$\langle L_C\rangle = \sqrt{\frac{2}{\pi}}\frac{P}{w_b}\theta_z \int_{-\infty}^{\infty} f(x) e^{-\frac{2x^2}{w_b^2}} dx - \mu P + \frac{P}{2w_b^2} + \sqrt{\frac{2}{\pi}}\frac{P}{2w_b}\theta^2 \int_{-\infty}^{\infty} f_x^2 e^{-\frac{2x^2}{w_b^2}} dx + \frac{V_r P\left(1-e^{-\frac{w_b^2}{2}}\right)}{2} + \frac{\sqrt{2}A_{\rm NL}P w_{\rm NL}}{\left(2w_{\rm NL}^2+w_b^2\right)^{1/2}} - \frac{\sqrt{\pi}\sigma A_{\rm NL}^2}{2\sqrt{2}w_{\rm NL}} - \frac{\sqrt{\pi}w_{\rm NL}A_{\rm NL}^2}{2\sqrt{2}}. \tag{14}$$

The first term on the right-hand side (RHS) of Eq. (14) vanishes owing to the antisymmetry of $f(x)$. Using Eq. (13), variational equations are obtained for each variable parameter. The RHS of Eq. (13) is nonzero only for $\beta = \theta$ because $f(x)$ is the only odd function; the substitution of Eq. (14) into Eq. (13) provides

$$\theta = -2V_i \frac{\mathrm{Re}\left[\int_{-\infty}^{\infty} \sin(2x) f(x) e^{-\frac{2x^2}{w_b^2}} dx\right]}{\int_{-\infty}^{\infty} f_x^2 e^{-\frac{2x^2}{w_b^2}} dx}. \tag{15}$$

Equation (15) clearly shows that the phase associated with the solution depends on the imaginary part of the refractive index V_i; it vanishes when the potential is purely real, eventually providing a flat-phase soliton.

Similarly, the variation of Eq. (13) with respect to $A_{\rm NL}$ and $w_{\rm NL}$ yields

$$w_{\rm NL}^2 = \frac{w_b^2 + 2\sigma + \sqrt{\left(w_b^2+2\sigma\right)^2 + 24\sigma w_b^2}}{4}, \tag{16}$$

in full analogy with a conservative system [40]. Figure 6(a) compares Eq. (16) with numerical solutions: the two approaches are in good agreement (flat behavior versus μ), except for a constant factor due to the different shapes of the nonlinear perturbation. Clearly, the variational approach is not able to model the broadening of $V_{\rm NL}$ near the band edge due to the presence of non-negligible tails in the actual soliton.

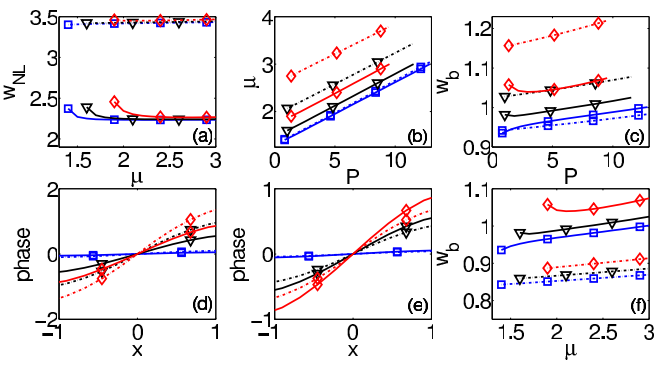

FIG. 6. (Color online) Graphs of (a) $w_{\rm NL}$ vs μ, (b) μ vs P, (c) w_b vs P, and (d) phase profile, calculated using the variational approach. (e) Phase profile and (f) w_b calculated using a simplified analytical approach (see text). In all panels $V_i = 0.1$ (□), $V_i = 1$ (▽), $V_i = 1.5$ (◇), and $\sigma = 10$. Solid lines correspond to numerics and dotted lines are variational (analytical) results.

The effects of the complex potential are apparent in the expressions for w_b,

$$\frac{1}{w_b^4} = \frac{V_r}{2}e^{-\frac{w_b^2}{2}} + \sqrt{\frac{2}{4\pi w_b^2}}\theta^2 \frac{\partial}{\partial w_b}\left(\frac{1}{w_b}\int_{-\infty}^{\infty} f_x^2 e^{-\frac{2x^2}{w_b^2}} dx\right) - \frac{2w_{\rm NL}^3 P}{\left(2w_{\rm NL}^2+w_b^2\right)^2\left(\sigma+w_{\rm NL}^2\right)}, \tag{17}$$

and μ,

$$\mu = \frac{1}{2w_b^2} + \frac{V_r}{2}\left(1-e^{-\frac{w_b^2}{2}}\right) + \sqrt{\frac{2}{4\pi w_b^2}}\theta^2 \int_{-\infty}^{\infty} f_x^2 e^{-\frac{2x^2}{w_b^2}} dx + \frac{2w_{\rm NL}^3 P}{\left(2w_{\rm NL}^2+w_b^2\right)\left(\sigma+w_{\rm NL}^2\right)}. \tag{18}$$

Figure 4 suggests a hyperbolic tangent profile for the transverse phase distribution, i.e., $f(x)$. Therefore, we take $f(x) = \tanh(x)$ and plot the beam width using Eq. (17) for various P and V_i in Fig. 6(c). The propagation constant μ is evaluated using Eq. (18), as well, and is compared with numerical results in Fig. 6(b). The dependence on soliton power P and imaginary potential V_i matches in both cases: in fact, w_b increases with power owing to self-defocusing, whereas the soliton broadens with V_i because of the larger flux of particle to accommodate. Figure 6(d) plots the numerical and variational phase profiles for various V_i, with differences ascribable to the erroneous evaluation of w_b in the variational method: the substitution of w_b from numerics into Eq. (15) provides a nearly perfect agreement.

In the highly nonlocal limit we can get another set of simplified analytical formulas for w_b and μ. Following Ref. [46] we can set $V_{\rm NL} \approx V_{\rm NL}^{(0)} + V_{\rm NL}^{(2)}x^2$, with $V_{\rm NL}^{(0)} = \int G(-x')|\phi(x')|^2 dx'$ and $V_{\rm NL}^{(2)} = (V_{\rm NL}^{(0)} - |\phi(0)|^2)/(2\sigma)$. Thus, Eq. (3) provides

$$\frac{2}{w_b^4} = V_r - \theta^2 + V_{\rm NL}^{(2)}, \tag{19}$$

$$\mu = \frac{1}{w_b^2} + \frac{\theta^2}{2} + V_{\rm NL}^{(0)}, \tag{20}$$

and

$$\theta = \frac{2V_i}{1+\frac{2}{w_b^2}}; \tag{21}$$

the corresponding results are plotted in Figs. 6(e) and 6(f). The observed discrepancy in phase profile can be attributed to the fact that w_b calculated using this approach is shifted by a small constant value [Fig. 6(f)]. Using w_b from numerics in Eq. (21) yields a perfect agreement with the numerically evaluated phase profile.

IV. STABILITY AND DYNAMICAL EVOLUTION

A. Linear stability analysis

The stability of the calculated gap soliton can be addressed by considering the effect of small perturbations in the

form

$$\Psi(x,z) = [\phi(x) + p(x)e^{i\lambda_g z} + q(x)e^{-i\lambda_g^* z}]e^{-i\mu z}, \quad (22)$$

$$V_{\mathrm{NL}}(x,z) = V_{\mathrm{NL}}^{\mu}(x) + \Delta V_{\mathrm{NL}}(x,z), \quad (23)$$

where V_{NL}^{μ} is the nonlinear potential computed via Eq. (4), corresponding to the soliton $\phi(x)$ once the propagation constant μ, the degree of nonlocality σ, and the linear properties (i.e., V_r and V_i) of the structure are selected. In the perturbative limit, i.e., neglecting nonlinear terms stemming from the added perturbation, we obtain from Eqs. (3) and (4) the following linear eigenvalue problem:

$$\lambda_g p = [\boldsymbol{L} - iV_i(x)]p - \phi \boldsymbol{D}(\phi^* p + \phi q^*), \quad (24)$$

$$\lambda_g q^* = [-\boldsymbol{L} - iV_i(x)]q^* + \phi^* \boldsymbol{D}(\phi q^* + \phi^* p), \quad (25)$$

where we defined the operator $\boldsymbol{L} = 0.5\partial_x^2 - V_{\mathrm{NL}}^{\mu}(x) - V_r(x) + \mu$. Moreover, we introduced $\boldsymbol{D} = (1 - \sigma\partial_x^2)^{-1}$, capable of computing the field intensity from the nonlinear potential V_{NL}; in other words, $\boldsymbol{D}$ is the convolution between the Green function of Eq. (2) and the intensity profile.

The solution is stable if $\mathrm{Im}(\lambda_g) = 0$ holds for all the eigenvalues, i.e., if the system has only real eigenvalues. The existence of complex eigenvalues corresponds to an oscillatory instability with $\mathrm{Im}(\lambda_g) > 0$ (<0), the latter implying exponentially decaying (growing) modes together with intensity oscillations while the wave evolves along z. We solved the system of Eqs. (24) and (25) using pseudospectral techniques based on Chebyshev polynomials to compute both the diffraction operator and the operator $\boldsymbol{D}$. We chose a grid extending to 40 along x (much larger than the maximum degree of nonlocality used, i.e., $\sigma = 10$) to avoid artifacts. The grid consisted of 1001 points, the latter ensuring independence from the numerical resolution for both the eigenvalues and the eigenfunctions in the range of interest (see below).

As a first attempt, we solved the system of Eqs. (24) and (25) for $V_i = 0$ and any degree of nonlocality: in agreement with previous works [40], gap solitons are stable (that is, $|\mathrm{Im}(\lambda_g)|$ is less than 10^{-13}, well below our numerical accuracy) for every σ and μ. Next, we considered $V_i \neq 0$. In the Kerr case ($\sigma = 0$) we find solitons are unstable, as briefly described in Ref. [27]; here we want to address the role played by nonlocality in soliton stability. Figure 7 illustrates the behavior of λ_g versus the gain and loss coefficient V_i and the soliton propagation constant μ. The values of $\mathrm{Re}(\lambda_g)$ are limited to the interval $[-6\ 6]$, as values outside it are associated with high-frequency noise. First, regardless of the soliton and structure parameters, there is an oscillatory instability due to the ubiquitous presence of eigenvalues with nonvanishing real as well as imaginary parts. Moreover, all the eigenvalues responsible for the OI appear in quartets, featuring the same $|\mathrm{Im}(\lambda_g)|$ and $|\mathrm{Re}(\lambda_g)|$ [47]. The eigenvalue distribution is quite complex; nevertheless, some general trends can be observed. For $V_i = 0.1$ the OI eigenvalues are located close to the origin of the complex plane, whereas for higher V_i new branches of OI eigenvalues appear, stemming from the broken degeneracy of the purely real eigenvalues. We also note that a new quartet of OI eigenvalues appears for $V_i \geqslant 0.5$, with $|\mathrm{Re}(\lambda_g)|$ close to 4.

The trend of the instability versus V_i and μ can be assessed by looking at Fig. 8. To completely study the instability we computed the eigenvalues having the largest imaginary part

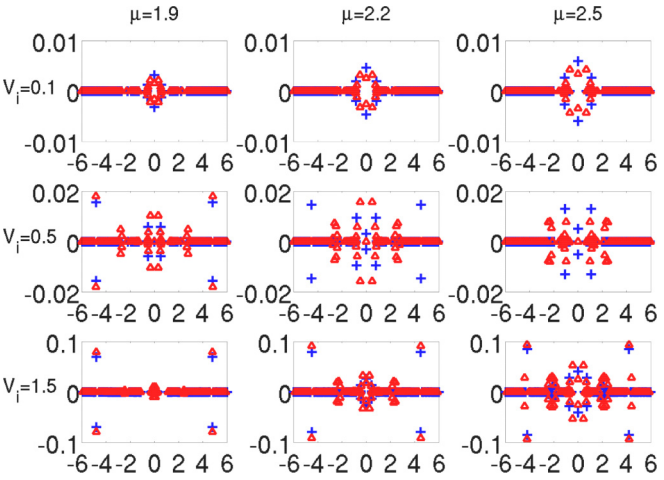

FIG. 7. (Color online) Eigenvalues λ_g for various μ (i.e., soliton power) and imaginary potential V_i in the complex plane (the horizontal axis corresponds to the real part, the vertical axis to the imaginary one). Blue + and red △ correspond to $\sigma = 1$ and $\sigma = 10$, respectively.

(i.e., the maximum growth rate) in the range $|\mathrm{Re}(\lambda_g)| \in [0\ 3]$ (we name it λ_1) and in the interval $|\mathrm{Re}(\lambda_g)| \in [3\ 8]$ (we name it λ_2). Let us start from λ_1: in general, the growth rate increases with μ, and at the same time $|\mathrm{Re}(\lambda_1)|$ gets larger, that is, the leading unstable mode moves away from the origin. The former statement always holds true except for $\sigma = 1$ and $V_i = 0.1$ or $V_i = 1.5$: in both these cases the real part of λ_1 vanishes; i.e., there is no OI. By looking at the growth rate, for $V_i = 1.5$ we see a rapid noise amplification, whereas for $V_i = 0.1$ $|\mathrm{Im}(\lambda_1)|$ is negligible; that is, the instability should be appreciable only over lengths much longer than the beam Rayleigh distance. Finally, we also note that the growth rate tends to increases with V_i.

The behavior of λ_2 is different. For low V_i the growth rate is zero for every nonlocality σ. The real part of λ_2 does not depend on V_i, whereas it drops off as μ increases. Interestingly, the growth rate associated with λ_2 is dominant with respect to

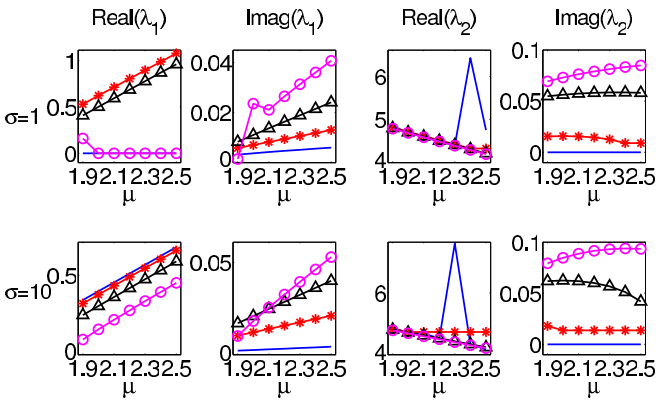

FIG. 8. (Color online) λ_1 and λ_2 vs μ, for $\sigma = 1$ (first row) and $\sigma = 10$ (second row). The imaginary potential V_i is 0.1 (blue lines without symbols), 0.5 (red lines with stars), 1.0 (black lines with triangles), and 1.5 (magenta lines with circles), respectively.

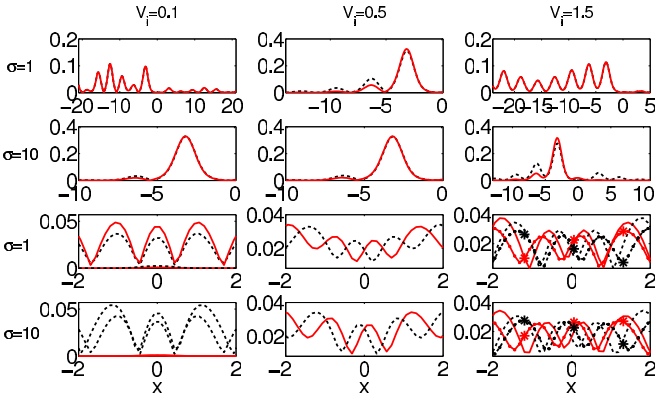

FIG. 9. (Color online) Spatial profile vs x of the eigenfunctions corresponding to the eigenvalues in Fig. 8. The first two rows correspond to λ_1, the other two rows to λ_2. In the first two rows, red solid and black dashed lines correspond to $|p(x)|$ [$q(x)$ is negligibly small compared with $p(x)$] for $\mu = 1.9$ and $\mu = 2.5$, respectively; in the plots we took only the modes with $\mathrm{Re}(\lambda_1) > 0$ and $\mathrm{Im}(\lambda_1) < 0$. In the third and fourth rows, for $V_i = 0.1$ red solid and black dashed lines correspond to $|p(x)|$ and $|q(x)|$, respectively; for larger V_i the red solid lines with and without symbols correspond to $|q(x)|$ for stable perturbations [$|p(x)|$ is not plotted as it has the same behavior], whereas the black dashed lines with and without symbols correspond to growing modes. Lines without and with symbols correspond to $\mu = 1.9$ and $\mu = 2.5$, respectively.

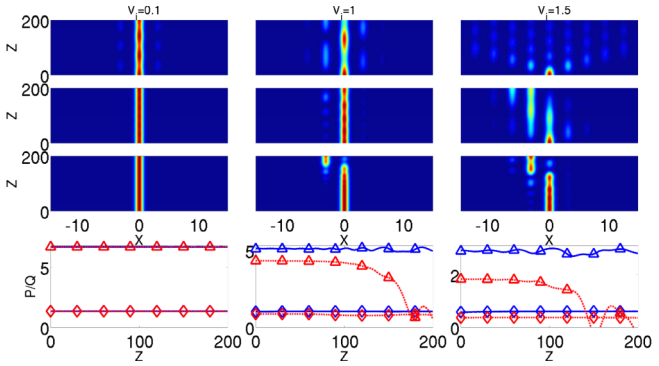

FIG. 10. (Color online) Intensity evolution in the plane xz when the shape of the input beam corresponds to the gap soliton, but with 0.25 of the soliton power (first row), 0.5 of the soliton power (second row), and 1.25 times the soliton power (third row); here we chose $\mu = 2$ and $\sigma = 10$. The last row illustrates the z evolution of parameters P (blue solid line) and Q (red dotted line) for powers 0.25 ($\diamond$) and 1.25 ($\triangle$).

λ_1 for large V_i (in Fig. 8 this occurs for both $V_i = 1$ and $V_i = 1.5$).

We can summarize our findings as follows: except for the cases discussed above, the instability rate grows with both V_i and μ. This relates to a breakup of the $\mathcal{PT}$ symmetry when a perturbation is added to the soliton, analogously to Ref. [21]. In fact, large V_i induce the appearance of a complex spectrum (see Fig. 1, for example); in a similar way, large μ correspond to lower real potentials trapping the wave, thus leading to a reduced effective $\mathcal{PT}$-breaking threshold.

To validate our interpretation of soliton stability, Fig. 9 graphs the eigenfunctions corresponding to the eigenvalues λ_1 and λ_2. For λ_1 the eigenfunctions $p(x)$ and $q(x)$ are strongly asymmetric with respect to $x = 0$: the eigenfunctions featuring a positive growth rate [i.e., $\mathrm{Im}(\lambda_1) < 0$] are centered around $x = -\pi$, i.e., on the adjacent channel with respect to the gap soliton; eigenfunctions featuring a negative growth rate corresponding to an exponential decay on propagation [i.e., for $\mathrm{Im}(\lambda_1) > 0$, not shown in Fig. 9] can be found by a mirror reflection with respect to $x = 0$. Moreover, the transverse phase profiles of $p(x)$ and $q(x)$ are nonuniform. All these properties confirm that the instability is due to the presence of perturbation modes breaking the $\mathcal{PT}$ symmetry: otherwise stated, the gap soliton propagates in a *sea* of unstable modes, excited by differences between the actual field profile and the exact soliton shape. The linear stability analysis (LSA) allows us to predict that the soliton instability takes place as an asymmetric transfer of power towards the gain regions (in our geometry $x < 0$), manifesting itself together with longitudinal oscillations in the field intensity due to the nonvanishing real part of λ_1.

For λ_2 the eigenfunctions are more complicated: for $V_i > 0.1$ they appear as delocalized Bloch waves (in Fig. 9 a zoom around $x = 0$ is plotted) with spatial frequency dictated by $\mathrm{Re}(\lambda_2)$ and conserving the main properties found for λ_1: asymmetry around $x = 0$, positive and negative growth rates, and a nonflat phase profile. A difference exists due to their periodic profile along x: their shape is such that it is impossible to easily determine the drift direction, or its occurrence at all.

B. Evolution of nonsoliton solutions

Before proceeding with the dynamical stability analysis of the stationary solution, we investigate the trade-offs between diffraction, linear lattice, and self-defocusing nonlinearity on wave propagation by numerically integrating Eq. (1) with a standard beam propagation method (BPM); we use splitting of the propagation operator and a Crank-Nicolson scheme for the diffraction term. We launch in the nonlinear lattice a wave packet with spatial distribution corresponding to a gap soliton, but varying its input amplitude. This approach corresponds to adding low-frequency noise to the soliton. We start with an input excitation which is one quarter of the soliton power; Fig. 10 (top row) plots the corresponding numerical results. Discrete diffraction is observed, with the linear $\mathcal{PT}$-symmetric potential introducing a left-right asymmetry in the intensity distribution owing to the nonreciprocity of the Bloch-Floquet modes [21].

Accordingly, the asymmetry becomes prominent as the imaginary part of the refractive index V_i gets larger (compare different columns in Fig. 10). The complex potential also results in longitudinal oscillations of the beam intensity versus propagation, in agreement with the presence of OI. A further increase in power to half that of the soliton reduces diffraction, but for increasing V_i the symmetry in propagation is broken and the beam diffracts only in one direction (second row of Fig. 10). Increments in excitation reduce discrete diffraction until, when the power corresponds to the exact soliton, the wave-packet profile along z becomes invariant; noteworthy, in agreement with Fig. 4, the larger V_i is the larger is the amount of power coupled to adjacent guides owing to a lower linear confinement.

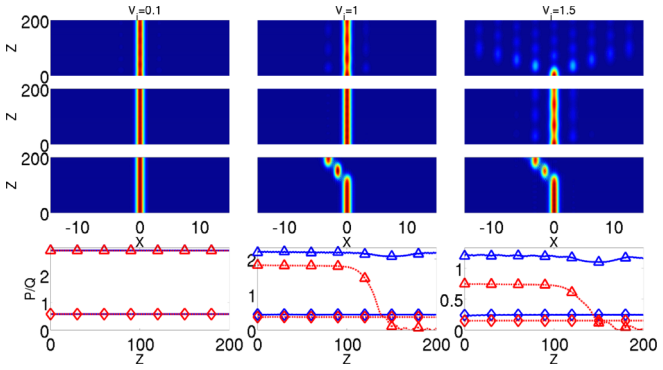

FIG. 11. (Color online) Same as in Fig. 10 but with $\sigma = 1$.

For powers above soliton generation (Fig. 10, third row), self-defocusing becomes comparable with the linear trapping potential V_r, until eventually a power-dependent breaking of $\mathcal{PT}$ symmetry (see Fig. 1) occurs and, consequently, a strong left-right asymmetry [21]. The net effect is a transverse motion of the nonlinear wave packet from one channel to the other, the direction dictated by V_i: the wave is attracted towards the gain region [in our case (see Sec. II) negative x]; this is in perfect agreement with the LSA carried out in Sec. IV A.

Even though the LSA is formally valid only for small perturbations, its results can describe other minor features of the wave evolution: the oscillation period increases with V_i (LSA predicts a period of about 60 for $V_i = 1.5$, in agreement with BPM simulations) and the exponential growth gets larger with V_i as well (for $V_i = 1.5$ LSA predicts an increase equal to e over a length of 50, in agreement with BPM). The LSA can also account for the small excitation of the adjacent guide on the right-hand side (i.e., towards the loss region) for large V_i (see the third panel in the second row of Fig. 9).

Finally, Fig. 10 graphs the quantity Q, defined as the quasipower $Q = \int \Psi(x,z)\Psi^*(-x,z)dx$ which is conserved in the linear regime [21] together with the real power P: the power is almost conserved everywhere, whereas Q changes strongly when the $\mathcal{PT}$ symmetry is broken due to the nonlinear response.

It is also important to understand the role played by nonlocality. To this extent, we repeated the simulations in Fig. 10 for a lower nonlocality, in particular for $\sigma = 1$, as displayed in Fig. 11: in agreement with the LSA, in this case the gap soliton is slightly more stable, with a trend opposite to that of solitons for $V_i = 0$, both in the discrete [17] and in the continuous cases [46].

The wave-packet behavior versus input power can be explained by resorting to particle conservation, as expressed by Eq. (8). After recasting the divergence of the flux j as $(\partial\rho/\partial x)\partial\chi/\partial x + \rho\partial^2\chi/\partial x^2$, the particle conservation expressed by Eq. (8) provides $\partial\rho/\partial z > 0$ when

$$\frac{\partial^2\chi}{\partial x^2} + \frac{1}{\rho}\frac{\partial\rho}{\partial x}\frac{\partial\chi}{\partial x} < 2V_i(x). \tag{26}$$

According to Fig. 4, corresponding to the soliton we can set $\chi(x) \approx c_0 x$; i.e., the phase follows a linear trend across x, with c_0 a constant proportional to V_i. From the figure we find $c_0 > 0$. Equation (26) turns into $(c_0/\rho)\partial\rho/\partial x < 2V_i(x)$. First, we note that the amplitude change cancels out due to the linearity of the conservation equation in ρ. Second, due to self-defocusing nonlinearity, powers exceeding the soliton case yield a broadening of the soliton intensity profile ρ (see Fig. 6), with a diminished absolute value of the derivative of ρ. This means that condition (26) is satisfied for $x < 0$ (gain region), whereas it is broken for $x > 0$ (loss region). In other words, particles undergo accumulation in the gain region and depletion in the loss region due to the imbalance of the flux j.

Let us now consider how this affects power coupling between adjacent guides. The accumulation of particles on the left of the core guide increases the net number of particles tunneling to the next channel, this being enhanced by the defocusing character of the nonlinearity, i.e., by lowering of the Peierls-Nabarro barrier. Conversely, in self-focusing media the particle flux outwards is reduced by the nonlinearity; hence, gap solitons are stable [15]. The opposite phenomenon takes place on the right-hand side, with particles moving to the core guide from the lateral guide. Summarizing, the net effect is a particle motion towards negative x. Noteworthy is that the field increase towards the lateral guide progressively reduces the nonlinear dephasing between them, allowing a partial back-coupling of power towards the input guide and thus inducing the oscillatory instability. The simulations demonstrate that, over several cycles, the particles tend to acquire a net motion towards negative x. Analogous phenomena occur for powers below soliton formation, but with beam broadening due to diffractive spreading.

The explanation just provided agrees with both LSA and BPM results: the instability of gap solitons is related to the transverse flux of the particle; thus, it is very small for low V_i (gap solitons for $V_i = 0$ are stable) whereas it is enhanced as the size of the gain-to-loss ratio is bigger. Additionally, flux considerations allow us to understand the dependence of soliton stability on nonlocality: a higher nonlocality yields narrower solitons, that is, larger $\partial\rho/\partial x$, in turn increasing the flux j.

C. BPM study of noise effects on soliton propagation

Next we analyze the dynamical stability of propagating gap solitons by adding Gaussian noise at the input section $z = 0$ with a magnitude corresponding to 0.01% of the soliton amplitude. For low V_i LSA predicts $|\mathrm{Im}(\lambda_g)|$ on the order of 10^{-3}; that is, the instability should appear for propagation lengths larger than 10^3 (blue solid lines in Fig. 8). (For the sake of comparison with the linear regime, discrete diffraction induces an appreciable spreading at $z = 20$.) The numerical simulations do not show appreciable changes in soliton profile up to $z = 200$, thus confirming the LSA results, regardless of the value of μ (first two columns in Figs. 12 and 13). For larger V_i LSA predicts a much higher growth rate, comprising oscillations in the intensity evolution versus z and growing modes for all σ: the numerical results in the last two columns of Figs. 12 and 13 confirm the predictions. Consistently with the LSA, the simulations demonstrate that, for μ closer to the edge of the bottom band, the soliton stability improves more than for μ closer to the edge of the top band; i.e., the growth rate increases with μ.

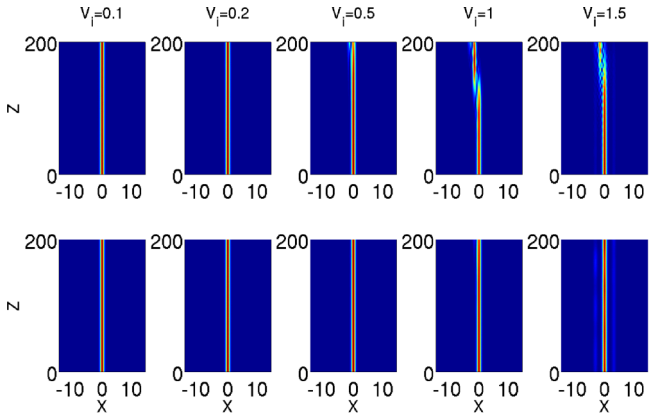

FIG. 12. (Color online) Evolution of stationary solutions in the plane (x,z) for $\mu = 1.9$. The soliton was heavily perturbed by noise with standard deviation 0.01 added to the input for $\sigma = 1$ (top) and $\sigma = 10$ (bottom), respectively, for various V_i as marked.

The LSA predicts similar instability lengths for solutions with different σ and large V_i, with instability in general increasing as nonlocality becomes larger, the latter finding being confirmed in the presence of low-frequency noise; see Sec. IV B. Conversely, BPM simulations shown in Figs. 12 and 13 indicate that the instability drops off when nonlocality is increased, but confirm the small dependence of the growth rate from nonlocality. The observed behavior can be explained in the context of LSA: when we add high-frequency noise, we are exciting unstable modes with large $\mathrm{Re}(\lambda_g)$ (larger than 8, thus out of the range plotted in Fig. 7), encompassing a complicated distribution of the eigenvalues versus nonlocality. The last statement is confirmed by the high-frequency variations in the intensity distribution in Figs. 12 and 13 in comparison with the smooth behavior followed in Figs. 10 and 11.

Finally, Fig. 14 provides an estimation of the instability behavior, plotting the value of V_i at which the instability manifests on a distance lower than 200, when a soliton perturbed with a noise of constant amplitude (0.01), regardless of the nonlocality parameter σ and of the propagation constant μ. As discussed previously, instability increases both with V_i and μ; at the same time, broader nonlinear response helps in inhibiting soliton blow-up.

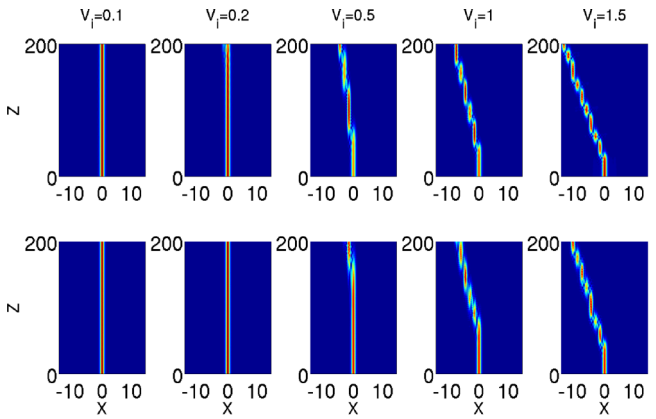

FIG. 13. (Color online) Same as in Fig. 12 but for $\mu = 3$.

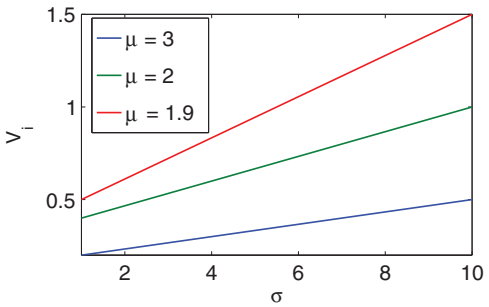

FIG. 14. (Color online) Magnitude of the imaginary potential V_i at which instability occurs for various nonlocality strengths σ and increasing μ (top to bottom curves). Solitons remain stable for a larger range of V_i when μ is lower.

V. CONCLUSIONS

In conclusion, we investigated the shape, existence curve, and stability of $\mathcal{PT}$-symmetric gap solitons in a self-defocusing medium featuring a nonlocal nonlinearity and a linear periodic potential. We showed that fundamental gap solitons exist inside all the first band gap, with appreciable tails in proximity of the top of the lowest band edge. As in the absence of gain or loss, the magnitude of the tails decreases as the nonlocal range broadens; moreover, for a given propagation constant, a higher nonlocality requires higher powers to form a soliton. We also demonstrated that solitons possess real and imaginary parts in order to conserve particle number, with the imaginary part proportional to gain or loss terms. A variational approach suitable for the study of $\mathcal{PT}$-symmetric solutions was developed, as well as an analytical method in the highly nonlocal limit, confirming the same dependence of soliton features on system parameters as shown by exact numerical solutions. We found that, in the presence of an imaginary potential, gap solitons become oscillatory unstable. Moreover, using both a linear stability analysis and BPM simulations, we showed that the perturbation growth rate changes dramatically with the imaginary potential: for large gain or loss terms the soliton shape is conserved over much shorter distances than in the case of small imaginary potentials (much shorter than the characteristic discrete diffraction length). The instability manifests mainly as a transverse particle flux (photons in the electromagnetic case) across the periodic lattice, with soliton motion towards the gain region. We also demonstrated that instability slightly changes with the response width of the nonlinearity, with the behavior being strongly dependent on the spectral contents of the applied perturbation. Finally, we demonstrated that solitons closer to the lower band edge, i.e., with lower μ, are more stable than those with high μ, the former solitons being well within the region where $\mathcal{PT}$ symmetry is fulfilled. Last, our findings can find application, for example, in the power-driven control of optical signals into a waveguide array.

ACKNOWLEDGMENTS

J.C.P. gratefully acknowledges FCT Grant No. SFRH/BPD/77524/2011 for support and thanks YuanYao Lin for useful discussion.

[1] C. M. Bender and S. Boettcher, Phys. Rev. Lett. **80**, 5243 (1998).
[2] C. M. Bender, Contemp. Phys. **46**, 277 (2005).
[3] A. Guo, G. J. Salamo, D. Duchesne, R. Morandotti, M. Volatier-Ravat, V. Aimez, G. A. Siviloglou, and D. N. Christodoulides, Phys. Rev. Lett. **103**, 093902 (2009).
[4] C. M. Bender, S. Boettcher, and P. N. Meisinger, J. Math. Phys. **40**, 2201 (1999).
[5] H. Ramezani, D. N. Christodoulides, V. Kovanis, I. Vitebskiy, and T. Kottos, Phys. Rev. Lett. **109**, 033902 (2012).
[6] J. Schindler, Z. Lin, J. M. Lee, H. Ramezani, F. M. Ellis, and T. Kottos, J. Phys. A: Math. Theor. **45**, 444029 (2012).
[7] H. Benisty, A. Degiron, A. Lupu, A. D. Lustrac, S. Chénais, S. Forget, M. Besbes, G. Barbillon, A. Bruyant, S. Blaize, and G. Lérondel, Opt. Express **19**, 18004 (2011).
[8] N. Bender, S. Factor, J. D. Bodyfelt, H. Ramezani, D. N. Christodoulides, F. M. Ellis, and T. Kottos, Phys. Rev. Lett. **110**, 234101 (2013).
[9] G. Castaldi, S. Savoia, V. Galdi, A. Alù, and N. Engheta, Phys. Rev. Lett. **110**, 173901 (2013).
[10] N. Lazarides and G. P. Tsironis, Phys. Rev. Lett. **110**, 053901 (2013).
[11] C. E. Rüter, K. G. Makris, R. El-Ganainy, D. N. Christodoulides, M. Segev, and D. Kip, Nat. Phys. **6**, 192 (2010).
[12] A. Regensburger, C. Bersch, M.-A. Miri, G. Onishchukov, D. N. Christodoulides, and U. Peschel, Nature (London) **488**, 167 (2012).
[13] A. Regensburger, M.-A. Miri, C. Bersch, J. Näger, G. Onishchukov, D. N. Christodoulides, and U. Peschel, Phys. Rev. Lett. **110**, 223902 (2013).
[14] L. Feng, M. Ayache, J. Huang, Y.-L. Xu, M.-H. Lu, Y.-F. Chen, Y. Fainman, and A. Scherer, Science **333**, 729 (2011), http://www.sciencemag.org/content/333/6043/729.full.pdf.
[15] Z. H. Musslimani, K. G. Makris, R. El-Ganainy, and D. N. Christodoulides, Phys. Rev. Lett. **100**, 030402 (2008).
[16] C. Hang, G. Huang, and V. V. Konotop, Phys. Rev. Lett. **110**, 083604 (2013).
[17] F. Lederer, G. I. Stegeman, D. N. Christodoulides, G. Assanto, M. Segev, and Y. Silberberg, Phys. Rep. **463**, 1 (2008).
[18] A. Fratalocchi, G. Assanto, K. A. Brzdakiewicz, and M. A. Karpierz, Opt. Lett. **29**, 1530 (2004).
[19] C. Conti, S. Trillo, and G. Assanto, Phys. Rev. Lett. **85**, 2502 (2000).
[20] D. Mandelik, R. Morandotti, J. S. Aitchison, and Y. Silberberg, Phys. Rev. Lett. **92**, 093904 (2004).
[21] K. G. Makris, R. El-Ganainy, D. N. Christodoulides, and Z. H. Musslimani, Phys. Rev. Lett. **100**, 103904 (2008); Phys. Rev. A **81**, 063807 (2010); Int. J. Theor. Phys. **50**, 1019 (2011).
[22] S. V. Dmitriev, A. A. Sukhorukov, and Y. S. Kivshar, Opt. Lett. **35**, 2976 (2010).
[23] N. V. Alexeeva, I. V. Barashenkov, A. A. Sukhorukov, and Y. S. Kivshar, Phys. Rev. A **85**, 063837 (2012); I. V. Barashenkov, S. V. Suchkov, A. A. Sukhorukov, S. V. Dmitriev, and Y. S. Kivshar, *ibid.* **86**, 053809 (2012); I. V. Barashenkov, L. Baker, and N. V. Alexeeva, *ibid.* **87**, 033819 (2013).
[24] J. Zeng and Y. Lan, Phys. Rev. E **85**, 047601 (2012).
[25] H. Li, X. Jiang, X. Zhu, and Z. Shi, Phys. Rev. A **86**, 023840 (2012).
[26] S. Hu, D. Lu, X. Ma, Q. Guo, and W. Hu, Eur. Phys. Lett. **98**, 14006 (2012).
[27] S. Nixon, L. Ge, and J. Yang, Phys. Rev. A **85**, 023822 (2012).
[28] Z. Shi, H. Li, X. Zhu, and X. Jiang, Eur. Phys. Lett. **98**, 64006 (2012).
[29] A. Piccardi, A. Alberucci, N. Tabiryan, and G. Assanto, Opt. Lett. **36**, 1356 (2011).
[30] C. Conti, A. Fratalocchi, M. Peccianti, G. Ruocco, and S. Trillo, Phys. Rev. Lett. **102**, 083902 (2009).
[31] D. Suter and T. Blasberg, Phys. Rev. A **48**, 4583 (1993).
[32] I. V. Barashenkov, M. M. Bogdan, and V. I. Korobov, Europhys. Lett. **15**, 113 (1991).
[33] A. De Rossi, C. Conti, and S. Trillo, Phys. Rev. Lett. **81**, 85 (1998).
[34] I. V. Barashenkov, D. E. Pelinovsky, and E. V. Zemlyanaya, Phys. Rev. Lett. **80**, 5117 (1998).
[35] Y.-Y. Lin, R.-K. Lee, and B. A. Malomed, Phys. Rev. A **80**, 013838 (2009).
[36] M. Johansson and Y. S. Kivshar, Phys. Rev. Lett. **82**, 85 (1999).
[37] A. Alberucci and G. Assanto, J. Opt. Soc. Am. B **24**, 2314 (2007).
[38] C. Kittel, *Introduction to Solid State Physics* (Wiley, New York, 1995).
[39] B. Midya, B. Roy, and R. Roychoudhury, Phys. Lett. A **374**, 2605 (2010).
[40] Y. Y. Lin, C. P. Jisha, C.-J. Jeng, R.-K. Lee, and B. A. Malomed, Phys. Rev. A **81**, 063803 (2010).
[41] N. K. Efremidis, Phys. Rev. A **77**, 063824 (2008).
[42] Z. Xu, Y. V. Kartashov, and L. Torner, Phys. Rev. Lett. **95**, 113901 (2005).
[43] S. Chvez Cerda, S. Cavalcanti, and J. Hickmann, Eur. Phys. J. D **1**, 313 (1998).
[44] C. P. Jisha, V. C. Kuriakose, and K. Porsezian, Phys. Rev. E **71**, 056615 (2005).
[45] A. Ankiewicz, N. Akhmediev, and N. Devine, Opt. Fiber Technol. **13**, 91 (2007).
[46] A. W. Snyder and D. J. Mitchell, Science **276**, 1538 (1997).
[47] P. G. Kevrekidis, D. J. Frantzeskakis, B. A. Malomed, A. R. Bishop, and I. G. Kevrekidis, New J. Phys. **5**, 64 (2003).